IEEE Open Journal of Antennas and Propagation

Received XX Month XXXX; revised X Month XXXX; accepted XX Month XXXX. Date of publication XX Month XXXX; date of current version XX Month XXXX.

Digital Object Identifier 10.1109/OAJPE.2020.2976889

Design of Wideband Reflectarray and Transmitarray Antennas With Low Sidelobe and Cross-Polarization Levels Using a Multifunctional Ultrathin Metasurface

Yufang Wang[1], Student Member, IEEE, Yuehe Ge[1], Senior Member, IEEE, Zhizhang (David) Chen[1,2], Fellow, IEEE, and Ziheng Zhou[1], Member, IEEE

[1]College of Physics and Information Engineering, Fuzhou University, Fuzhou 350108, China

[2]Department of Electrical and Computer Engineering, Dalhousie University, Halifax, NS B3H 4R2, Canada

CORRESPONDING AUTHOR: Yuehe Ge (e-mail: yuehe@ieee.org).

ABSTRACT Ensuring a low cross-polarization level (CPL) is imperative in the design of antennas with a low sidelobe level (SLL). This paper introduces an innovative approach for designing wideband, high-gain, low-sidelobe, and low-cross-polarization reflectarray (RA) and transmitarray (TA) antennas. The methodology leverages a groundbreaking metasurface endowed with the capability for independent amplitude and phase manipulation in both transmission and reflection modes. Initial characterization robustly verifies the metasurface's proficiency in independently controlling amplitude and phase in reflection and transmission modes. Importantly, the study demonstrates that this metasurface enables the straightforward attainment of low CPL in the design of low-SLL RA and TA antennas. The study progresses to the design, fabrication, and testing of three RA and TA antennas. The obtained simulated and measured results affirm their exceptional performance in terms of wideband, high-gain, low-SLL, and low-CPL characteristics.

INDEX TERMS Metasurface, amplitude and phase control, sidelobe level, cross-polarization level, transmitarray, reflectarray

I. INTRODUCTION

Antennas serve as indispensable elements in wireless systems, playing a pivotal role in their functionality. When it comes to antenna design, parameters such as gain, sidelobe level (SLL), and bandwidth stand out as critical metrics for assessing performance. The significance of these parameters varies across different applications, with each emphasizing specific aspects. For instance, in conventional military radar systems, the demand for anti-interference necessitates the deployment of radar antennas characterized by high gain and low sidelobe levels. Consequently, various techniques have been developed, as documented in references [1]-[10], to address the intricate task of designing antennas or arrays with low sidelobe levels.

Sidelobe manipulation techniques are commonly employed in waveguide slot array antennas [5]-[7] and traditional phased array antennas [8]-[10], where amplitude control is easily achievable. A high-gain, low-SLL substrate-integrated-waveguide slot array antenna was developed using the genetic algorithm (GA) technique, coupled with Schelkunoff's unit circle technique [7]. However, the achieved design exhibited a narrow bandwidth. In recent decades, planar phased array antennas have gained widespread usage. Despite their prevalence, obtaining low SLLs with these antennas is more challenging compared to the aforementioned waveguide slot array antennas. This challenge arises due to their reliance on a large number of antenna elements and complex feeding networks. In [10], a feeding network structure featuring multiple power divisions is proposed, facilitating amplitude distribution to achieve low sidelobe levels. The antenna attains a peak gain of 27.9 dBi, with sidelobe levels consistently below -20 dB.

In recent years, scholars have increasingly focused on metasurfaces due to their distinctive ability to manipulate the amplitude, phases, and polarization of electromagnetic (EM) waves. Notably, metasurfaces offer advantages such as low loss, a slim and compact profile, flexible design options, and straightforward fabrication processes [11]. Comparable to traditional planar phased arrays [12], [13], metasurfaces exhibit the capability for spatial phase variation, obviating the need for intricate phase-shifting networks. Consequently, they

have emerged as viable alternatives to phased array antennas for designing high-performance antennas, especially those intended for focused applications [14]. Different from the curved structures associated with traditional focusing antennas like reflector antennas and lens antennas, researchers have leveraged metasurfaces in the creation of reflectarray (RA) [15], [16], and transmitarray (TA) antennas [17]-[20]. These antennas offer advantages such as planar structures, high efficiencies, broad bandwidths, and the ability to control amplitude, phase, and polarization.

The reduction of SLLs in metasurface array antennas primarily involves two approaches: phase correction [21], [22], and amplitude control [23], [24]. In the pursuit of high-gain performance, [21] employs the normal phase compensation technique, leveraging the inherently tapered amplitude of the feed to achieve an impressive SLL of -20 dB. Extending this strategy, amplitude control is introduced to further suppress SLL in metasurface TA/RA antennas [23], [24], [29], [30]. In the study presented in [23], an amplitude-adjustable metasurface TA antenna achieves an SLL of -20 dB under plane wave illumination. Combining the two approaches, a circularly polarized low-SLL metasurface antenna is proposed in [24], where a phase controllable metasurface and an amplitude controllable metasurface are stacked, resulting in a remarkable SLL of -23.4 dB.

More recently, the emergence of multifunctional metasurfaces (MFMs) has expanded the realm of possibilities, encompassing simultaneous manipulation of amplitude and phase [25]-[30], as well as the execution of both reflecting and transmission functionalities [31]-[34]. These innovations have found applications in the design of antennas endowed with special functions [34], contributing to enhanced overall antenna performance, including SLL reduction [29], [30]. For instance, in [29], a RA antenna with simultaneous amplitude and phase control achieves an impressive SLL reduction to -25.6 dB. However, it introduces a challenge by converting redundant fields into cross-polarization ones due to amplitude control, thereby elevating cross-polarization levels (CPLs) within the operational space. Additionally, it's noteworthy that the metasurfaces developed in these studies exhibit the capability to control amplitude and phase in either transmission or reflection space, showcasing a current limitation in their functionality.

This paper introduces a cutting-edge, wideband, high-efficiency ultrathin metasurface with the unique capability to independently and precisely control amplitudes and phases in both transmission and reflection spaces [34]. The innovative metasurface has been preliminarily validated through elementary simulations, demonstrating its potential application in the design of low-SLL TA and RA antennas [35]. This study comprehensively presents the theory and methodology for designing wideband low-SLL TA and RA antennas, with a specific focus on achieving low-CPL performance, leveraging the unique attributes of the introduced metasurface. An exclusive advantage of this metasurface lies in its ability to ensure that, during the design

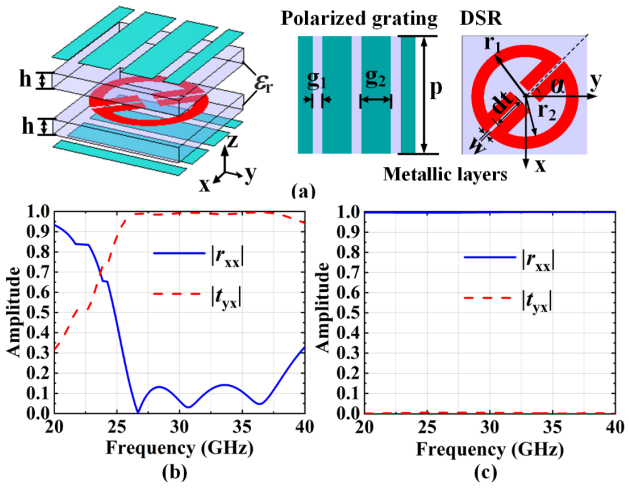

FIGURE 1. (a) Schematics of the multifunctional metasurface (MFM) element. The dimensions are p = 4 mm, h = 0.5 mm, g_1 = 0.33 mm, g_2 = 1 mm, r_1 = 1.7 mm, r_2 = 1.3 mm, dt = 1 mm, and w = 0.15 mm. (b) Transmission and reflection coefficients of the element under the x-polarized incident wave at α = ±45°. (c) Transmission and reflection coefficients at α = 0° or 90°.

of low-SLL RA antennas, redundant waves resulting from amplitude modulation pass through the metasurface, avoiding their retention in the working space and, consequently, preventing any adverse impact on the cross-polarization level within that space. Moreover, both TA and RA designs inherently exhibit low cross-polarization levels due to the presence of gratings on the top and bottom surfaces. Additionally, the modulation of transmission and reflection phases and amplitudes using the metasurface results in linearly varied phases and nearly unchanged amplitudes across a wide bandwidth. These novel properties collectively contribute to the development of wideband, high-gain, low-SLL, and low-CPL TA and RA antennas.

This paper is organized as follows: Section II characterizes the novel metasurface and highlights its distinctive properties, while Section III elucidates the strategy employed in designing low-SLL, low-CPL TA and RA antennas. Section IV presents the design, simulation, fabrication, and testing of various TA and RA antenna cases. Comparative analyses with counterparts from existing literature underscore the novel performance of the proposed designs, thus emphasizing the unique contributions of this paper. Finally, Section V draws conclusions based on the findings.

II. CHARACTERIZATION OF THE APPLIED METASURFACES

A. Element Design of the Concerned MFM

The structure of the MFM element under consideration is depicted in Fig. 1(a). This element comprises three metallic layers separated by two identical dielectric substrates with a dielectric constant (ε_r) of 4.5. The top and bottom metallic layers consist of two identical orthogonal polarized gratings that collectively form a Fabry-Perot cavity. Sandwiched between them is the middle metallic layer, serving as a dual-split-ring (DSR) polarizer, featuring a ring with dual

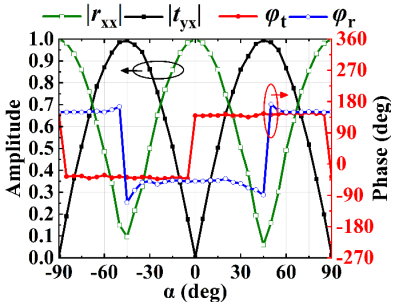

FIGURE 2. Characteristics of the MFM element. Co-polarization reflection ($|r_{xx}|$ and φ_r) and cross-polarization transmission ($|t_{yx}|$ and φ_t) versus α under x-polarized incident wave.

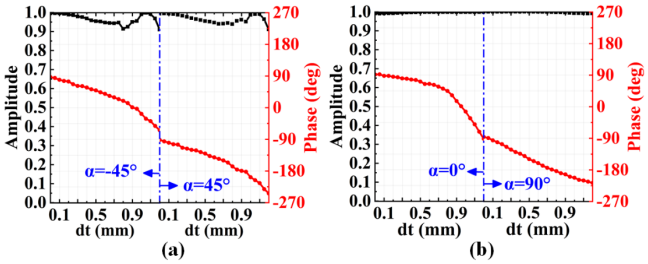

FIGURE 3. (a) Cross-polarization transmission amplitude ($|t_{yx}|$) and phase (φ_t) when α = ±45° and the parameter *dt* is changed from 0 mm to 1.2 mm. (b) Co-polarization reflection amplitude ($|r_{xx}|$) and phase (φ_r) when α = 0° and 90° and the parameter *dt* is changed from 0 mm to 1.2 mm.

symmetrical splits and four identical stubs. The operational principles of the DSR polarizer and the characteristics of the MFM element have been extensively discussed in [34]. The metasurface, employing this structure, is capable of achieving complete cross-polarization transmission (t_{yx}) at $\alpha = \pm 45°$ and complete co-polarization reflection (r_{xx}) at α = 0° or 90°, respectively. In the scope of this study, metasurface RA and TA antennas are designed at a frequency of 30 GHz. The initial phase involves the design of the MFM, and the ultimate geometric parameters of the MFM element are detailed in the caption of Fig. 1(a). The overall dimensions of the element measure 4×4×1 mm³ ($0.4\lambda \times 0.4\lambda \times 0.1\lambda$ at 30 GHz).

In Figs. 1(b) and 1(c), the simulated cross-polarization transmission at $\alpha = \pm 45°$ and co-polarization reflection at α = 0° or 90° are illustrated. It is evident that the metasurface exhibits functionality in both reflection and transmission modes, achieving an efficiency surpassing 90% within a bandwidth spanning from 23.7 to 39 GHz (48.8%). As detailed in [34], the amplitudes and phases of cross-polarization transmission and co-polarization reflection can be independently controlled by manipulating the rotation angle (α) and geometric parameters of the DSR, as visually demonstrated in Figs. 2 and 3.

Fig. 2 showcases the characteristics of cross-polarization transmission and co-polarization reflection with a continuously changing α. The transmission exhibits a dependence of $|sin(2\alpha)|$, while the reflection varies with a dependence of $|cos(2\alpha)|$ as α changes. The amplitudes of both transmission and reflection can be finely adjusted within the

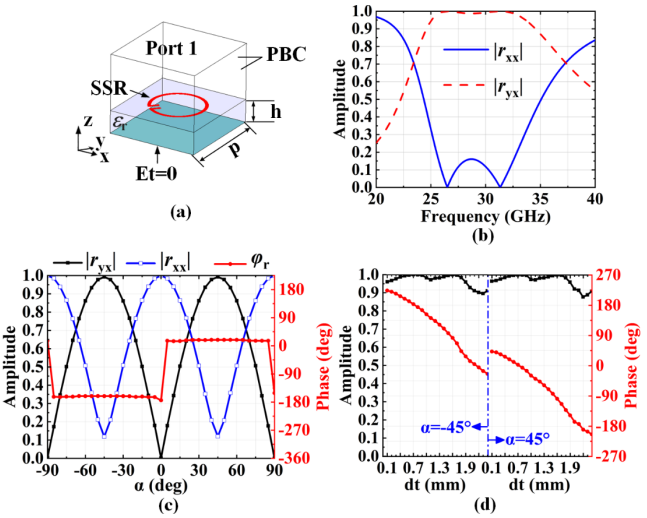

FIGURE 4. (a) Schematics of the full-reflection metasurface (FRM) element. (b) Reflection coefficients of the element under x-polarized incident wave at α = ±45°. (c) Cross-polarized reflection ($|r_{yx}|$ and φ_r) and co-polarized reflection amplitude($|r_{xx}|$) when the parameter α is changed. (d) Cross-polarized reflection amplitude ($|r_{yx}|$) and phase (φ_r) when α = ±45° and the parameter *dt* is changed from 0 mm to 2.4 mm. The fixed parameters are: r_1 = 1.3 mm, r_2 = 1.15 mm, w = 0.15 mm, h = 1mm, p = 4mm.

range [0,1] by varying α, with minimal phase shift—except for a phase jump of 180° when the amplitudes of transmission and reflection approach their minimum.

In Fig. 3, the amplitude and phase curves of the transmission and reflection are delineated concerning the parameter *dt*. In Fig. 3(a), depicting the transmission mode, a phase range of 0-180° is achieved at α = -45° by varying *dt* from 0 mm to 1.2 mm. Upon reaching α = 45°, a phase jump of 180° is introduced to the previously mentioned phase, resulting in an overall phase range of 360°. Fig. 3(b) illustrates a similar phase range achievable in the reflection mode.

These findings demonstrate the capability to attain the desired transmission and reflection amplitudes within the [0,1] range and phases spanning 0-360°. This is achieved by appropriately configuring the rotation angle α and the parameters of the dual-split-ring (DSR). With these phase and amplitude control capabilities, the EM waves on any part of the MFM can be precisely tuned, enabling intricate wavefront control in both transmission and reflection modes. It is crucial to highlight that these amplitude and phase controls can be executed across a wide bandwidth, as extensively detailed in [34]. Furthermore, the presence of gratings on both the top and bottom surfaces of the MFM generates highly pure polarizations in both transmission and reflection modes, resembling slot array antennas. Only EM with perpendicular linear polarizations to the metallic strips can be excited, contributing to the generation of TA and RA antennas with our proposed MFM that exhibit low cross-polarization levels.

B. Element design of the Full-Reflection Metasurface

In order to facilitate comparison, a full reflection metasurface (FRM) has been developed alongside the MFM. Fig. 4(a) illustrates a grounded single-split-ring (SSR) polarizer

employed in the FRM, resembling the split-ring (SR) design found in the DSR of the MFM (as detailed in Section II-A). The SSR polarizer features a single split connected to two stubs. Similar to MFM, the reflection element of the FRM achieves full cross-polarization reflection at $\alpha = \pm 45°$ with an efficiency exceeding 90% within the range of 24.4-34.6 GHz (34.5%), as illustrated in Fig. 4(b). The dependence of reflection amplitude and phase on the size (dt) of the SSR and the rotation angle (α) is portrayed in Fig. 4(c). As seen, varying α from -90° to 90° results in co- and cross-polarization reflections fluctuating within the [0,1] range, governed by the $|cos(2\alpha)|$ and $|sin(2\alpha)|$ dependencies, respectively. Except for a phase jump of 180° at $\alpha = 0°$, altering α does not influence the reflection phase. Fig. 4(d) illustrates that, as dt changes from 0 mm to 2.4 mm, the cross-polarization reflection phase (φ_r) covers the entire range of 0-360°, while cross-polarization reflection remains consistently above 0.85. Thus, amplitude and phase manipulation is achievable by adjusting both the rotation angle and the parameters of the reflection element.

Comparatively, the operation of the FRM, particularly in the reflection mode, exhibits slight differences from the MFM element discussed in Section II-A. In the FRM, variation in amplitude within the [0,1] range converts redundant power into cross-polarization within the same half-space due to the SSR polarizer. In contrast, the multifunctional metasurface, as depicted in Fig. 1(a), directs redundant power into the transmission space when modulating the reflection amplitude [34]. This distinction ensures that the electromagnetic waves in the reflection space remain undisturbed, as elucidated in the subsequent section.

In summary, we have characterized our concerned MFM for TA and RA applications, and the FRM specifically for the RA application. In instances where only phase control is necessary for either TA or RA applications, adjustments in the dimensions of the DSRs and SSRs become imperative while keeping the rotation angle (α) fixed. Conversely, in scenarios demanding only amplitude modulations for either TA or RA applications, the rotation angle (α) must be altered, rendering changes to the DSR/SSR dimensions unnecessary. Finally, when both amplitude and phase changes are required, a judicious adjustment of both the dimensions and rotation angle (α) of DSR/SSR is essential for optimal performance. This explanation provides clarity on the specific parameter adjustments based on the different design scenarios in TA and RA antenna applications.

III. THE STRATEGY OF SIDELOBE MANIPULATION IN ARRAY ANTENNAS

In this section, we integrate beam focusing and sidelobe reduction techniques to formulate the design of RA/TA antennas utilizing the configured metasurfaces as detailed in Section II. The primary objective of the beam focusing technique is to achieve a directive beam with substantial gain by converting the spherical incident wave, emanating from the feed source, into a planar wave. Building upon this foundation, the sidelobe reduction technique employs the Taylor synthesis

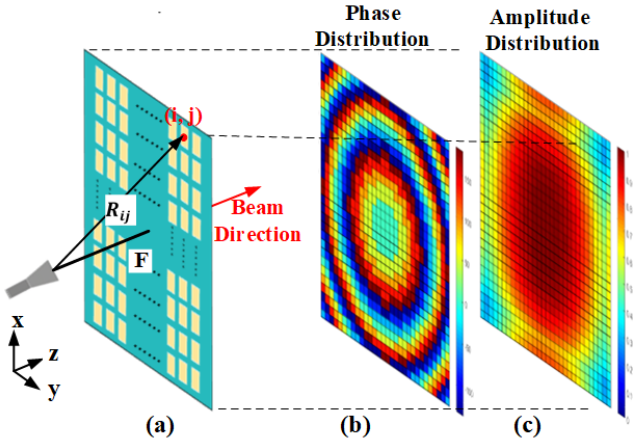

FIGURE 5. (a) Schematic of the TA antenna design. (b) Required phase distribution and (c) required amplitude distribution on the metasurface with 30×30 elements, where the goal of the amplitude control is determined with *SLL*<-30 dB.

method to finely control the amplitude distribution, thereby minimizing the SLLs.

A. The Beam focusing

The application of phase compensation is a standard approach in the design of TA and RA antennas. Illustrated in Fig. 5(a) are the schematics of the TA antenna. Employing the ray tracing method and the phase compensation technique, it is imperative that the phases of waves traversing the center and other designated positions of the TA antenna are precisely equal. This condition can be succinctly expressed as:

$$-k_0 F + \varphi_0 = -k_0 R_{ij} + \varphi_{ij} \quad (1)$$

where $k_0=2\pi/\lambda$ is the wave number in free space, φ_{ij} and φ_0 denote the compensation phases of elements located at the position (x_i, y_j) and the center of the transmitarray, respectively. The parameter F signifies the focusing distance between the phase center of the feed and the transmitarray, while R_{ij} represents the distance between the feed and the element positioned at the position (x_i, y_j) of transmitarray. The optimal focusing distance of the transmitarray is determined by the aperture size (D) and the 10-dB power beamwidth (θ_f) [13]:

$$F = D/\,2\,tan(0.5\theta_f) \quad (2)$$

Then the required compensation phases φ_{ij} are computed by:

$$\varphi_{ij} = k_0(\mathrm{R}_{ij} - F) \pm 2n\pi + \varphi_0, n \in N \quad (3)$$

where n is an integer number to ensure that the compensation phases are within [0°, 360°].

For the design of RA antennas, the offset feed is adopted to alleviate the influence of the feeding block, as shown in Fig. 6(a). The compensation phases on the RA can be calculated by [13]:

$$\varphi_{ij} = k_0(\boldsymbol{R_{ij}} - \boldsymbol{F} - \vec{\boldsymbol{r}}_{\boldsymbol{ij}} \times \hat{\boldsymbol{u}}_{\boldsymbol{0}}) + 2n\pi + \varphi_0 \quad (4)$$

where $\vec{r}_{ij}$ denotes the position vector of the element at the position (x_i, y_j) and $\hat{u}_0$ represents the unit vector of the main beam direction.

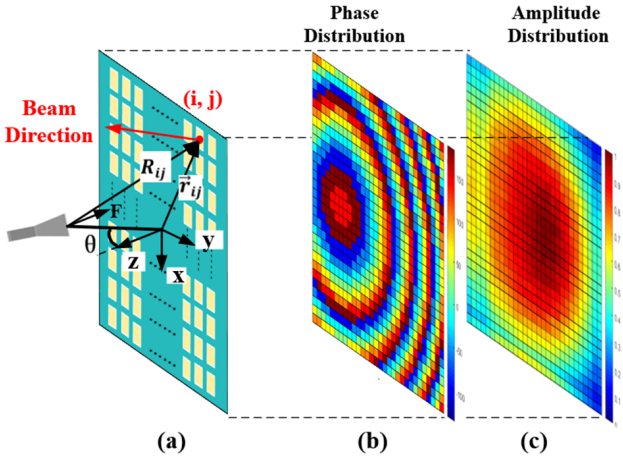

FIGURE 6. (a) Schematic of the RA antenna design. (b) Required phase distribution and (c) required amplitude distribution on the metasurface with 30×30 elements, where an offset feed is applied. The offset angle is 20º in the YOZ plane and the beam direction is 0º along the z-axis. The goal of the amplitude control is determined with *SLL*<-25 dB.

In practical applications, achieving continuous compensation phases can be challenging, leading to a common practice of utilizing discrete phases within the range of 0-360°. To address this, we have designed eight MFM/FRM elements, each dedicated to providing a specific compensation phase at intervals of 45°. In the scope of this study, the discrete compensation phases are specifically selected as follows:

$$\varphi_{ij} = \begin{cases} 0^\circ, & 0^\circ \le \varphi_{ij} < 45^\circ \\ 45^\circ, & 45^\circ \le \varphi_{ij} < 90^\circ \\ 90^\circ, & 90^\circ \le \varphi_{ij} < 135^\circ \\ 135^\circ, & 135^\circ \le \varphi_{ij} < 180^\circ \\ 180^\circ, & 180^\circ \le \varphi_{ij} < 225^\circ \\ 225^\circ, & 225^\circ \le \varphi_{ij} < 270^\circ \\ 270^\circ, & 270^\circ \le \varphi_{ij} < 315^\circ \\ 315^\circ, & 315^\circ \le \varphi_{ij} \le 360^\circ \end{cases} \quad (5)$$

B. The Sidelobe Reduction

The utilization of the Taylor synthesis method serves to manipulate the aperture amplitude distribution, allowing for effective control over the SLL [29]. In accordance with this method, the computation of one-dimensional Taylor distributions along the x- and y-axes, denoted by the column vectors T_x and T_y, respectively, is facilitated by the following equation [36]:

$$T(\mathrm{n}) = I_n(z_n) = 1 + 2\sum_{m=1}^{n-1} s(m, A, \bar{n})\cos(mp), n = 1,2,\dots,N \quad (6)$$

The comprehensive Taylor distribution across the two-dimensional surface for an array antenna is determined by T_x and T_y, amalgamated into a square matrix (T_{xy}) as depicted below:

$$T_{\mathrm{xy}} = T_x \cdot T_y' \quad (7)$$

The relationship governing the target aperture amplitude (T_{xy_ij}), the original excitation (I_{ij}), and the amplitude distribution (A_{c_ij}) of metasurface elements at the position (x_i, y_j) can be expressed as follows:

$$T_{xy\_ij} = I_{ij} \cdot A_{c\_ij} \quad (8)$$

Subsequently, the desired amplitude distribution of metasurface elements can be derived through the inversion of this formula. Acknowledging the challenge of continuous amplitude alteration, we discretize the amplitudes into ten distinct levels in this study, employing the following criteria:

$$A_{c\_ij} = \begin{cases} 1, & 0.9 \le A_{c\_ij} < 1 \\ 0.9, & 0.8 \le A_{c\_ij} < 0.9 \\ 0.8, & 0.7 \le A_{c\_ij} < 0.8 \\ 0.7, & 0.6 \le A_{c\_ij} < 0.7 \\ 0.6, & 0.5 \le A_{c\_ij} < 0.6 \\ 0.5, & 0.4 \le A_{c\_ij} < 0.5 \\ 0.4, & 0.3 \le A_{c\_ij} < 0.4 \\ 0.3, & 0.2 \le A_{c\_ij} < 0.3 \\ 0.2, & 0.1 \le A_{c\_ij} < 0.2 \\ 0.1, & 0 \le A_{c_{ij}} \le 0.1 \end{cases} \quad (9)$$

In accordance with the amplitude-phase modulation characteristics of MFM/FRM elements described in Section II, the transmission and reflection amplitudes can be adjusted within the range of [0,1] by solely manipulating the rotation angle (α) while the other structural parameters unchanged, as illustrated in Fig. 2. Consequently, the rotation angle (α) of metasurface elements can be determined using the following equation:

$$\alpha_{ij} = \alpha_{0\_ij} + \begin{cases} 0.5\cos^{-1}(A_{c\_ij}), & for\ MFM\ TA \\ 0.5\sin^{-1}(A_{c\_ij}), & for\ MFM\ RA \\ 0.5\cos^{-1}(A_{c\_ij}), & for\ FRM\ RA \end{cases} \quad (10)$$

where α_{0_ij} represents the initial rotation angle distribution on the metasurface for array antennas that solely employ phase control, without amplitude modulation.

IV. SIDELOBE MANIPULATION IN TA/RA ANTENNAS

In this section, we conduct three comparisons for transmitarray (TA) and reflectarray (RA) antennas, evaluating the performance under scenarios of phase control only and simultaneous amplitude and phase control. These comparisons aim to unveil the distinctive advantages of the multifunctional metasurface discussed in Section II.

A. Transmitarray Antennas with MFMs

The TA antenna configuration incorporates a metasurface TA utilizing the MFM elements, designed for operation in the transmission mode as detailed in Section II-A. The TA setup integrates a pyramidal horn with x-polarized feeding as a WR-28 standard, with the TA comprising 30 × 30 elements. Its aperture size measures 120 mm × 120 mm (equivalent to 12λ × 12λ at 30 GHz), and the thickness is 1 mm (0.1λ at 30 GHz). The F/D value, calculated by (4), is 0.83.

To provide a baseline for comparison, we initiate the design of a high-gain TA antenna solely employing phase control,

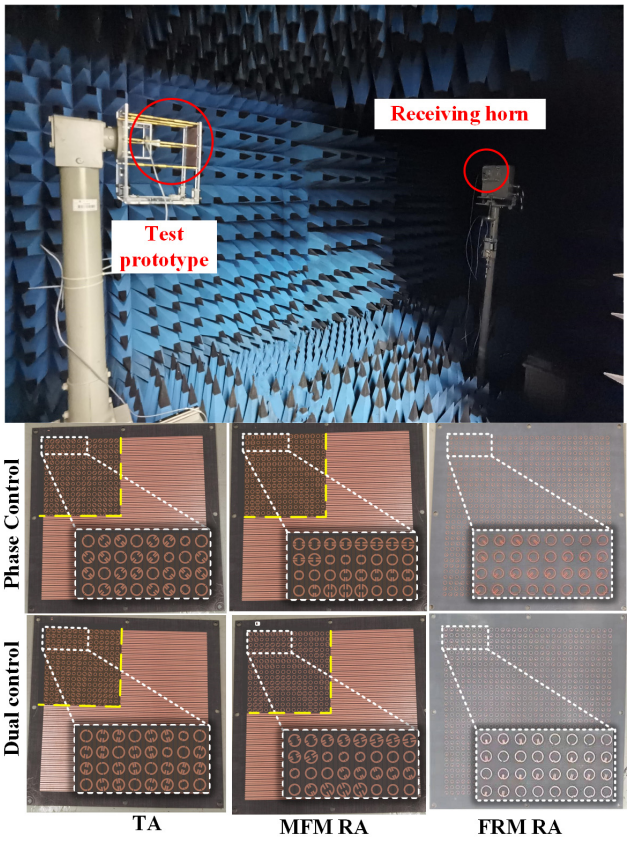

FIGURE 7. **Measurement setup and the metasurfaces prototypes.**

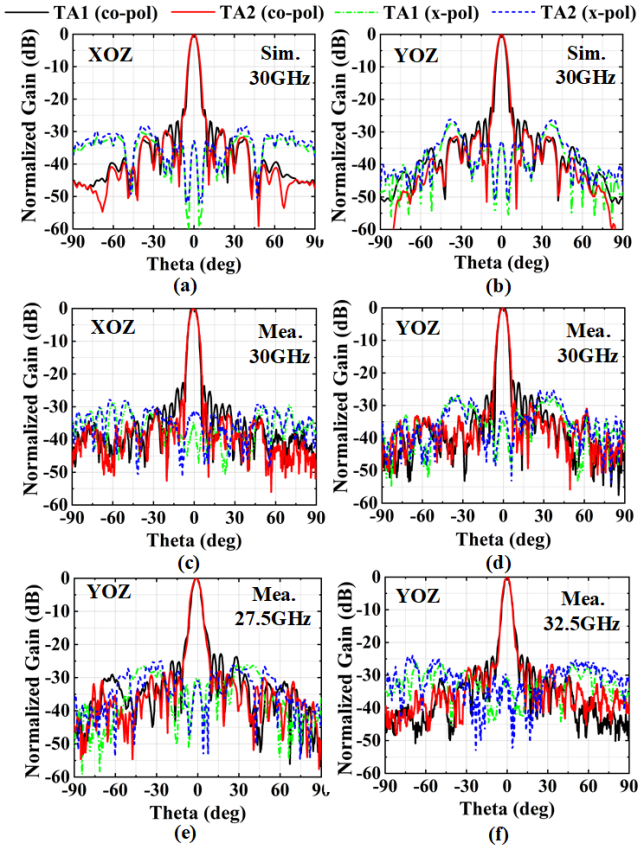

FIGURE 8. **Simulated radiation patterns at 30 GHz for TA antennas with phase control only (TA1) and both amplitude and phase control (TA2) in (a) XOZ plane and (b) YOZ plane. Measured radiation patterns for TA1 and TA2 (c) at 30 GHz in XOZ plane, (d) at 30 GHz in YOZ plane, (e) at 27.5 GHz in YOZ plane, (f) at 32.5 GHz in YOZ plane.**

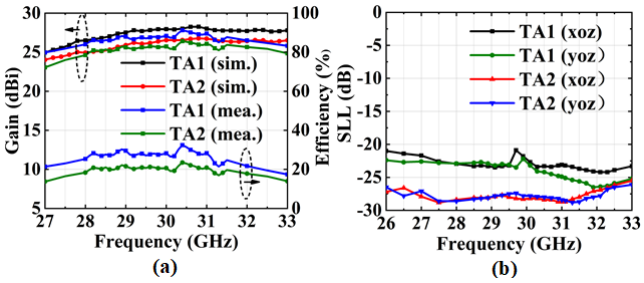

FIGURE 9. **(a) Simulated and measured gains and aperture efficiencies for the two TA antennas. (b) Measured SLLs of the two TA antennas with or without the amplitude control in XOZ plane and YOZ plane.**

without amplitude modulation. Specifically, the rotation angles of DSRs across the 30 × 30 MFM elements are set uniformly at ±45º. The required compensation phase distribution on the metasurface is determined by (5) and is presented in a discretized form in Fig. 5(b). Subsequently, the amplitude on the TA is converted into a Taylor distribution using the strategy outlined in Section III to suppress the SLLs. In the initial TA design (TA1), the amplitude distribution on the TA is derived from the illumination of the feeding horn, obtained through simulation in Ansys HFSS. The Taylor amplitude distribution on the TA is then determined according to (8) and (9), as depicted in Fig. 5(c). The objective of this design (TA2) is to achieve an SLL less than -30 dB. The rotation angles of all DSRs corresponding to the required transmission amplitudes are determined by (10), in accordance with the results presented in Fig. 2(a).

Both TA antennas underwent a comprehensive evaluation involving simulation in Ansys HFSS, fabrication using standard PCB techniques, and subsequent measurement in an anechoic chamber. Fig. 7 illustrates the metasurface prototypes and the measurement setup employed in this study. As can be seen, the rotation angles of DSRs in TA and SSRs in FRM RA with phase control are set at 45º, while those in MFM RA are either 0º or 90º. The reason is that only phase control is applied in these cases, given the exclusive application of phase control in these cases. However, the rotation angles of all DSRs in TA and MFM RA, as well as SSRs in FRM RA with dual control, full within the range of either $0^o<\alpha<90^o$ or $90^o<\alpha<180^o$. This variation is due to the modulation of either transmission or reflection amplitudes in these three scenarios. As illustrated in Figs. 2 and 4, the amplitude modulations in either transmission or reflection modes correspond to the rotation of the DSRs or SSRs.

The radiation patterns for the two TA antennas at 30 GHz, comparing simulated and measured results, are presented in Fig. 8. Notably, both TA antennas demonstrate well-defined pencil-shaped beams.

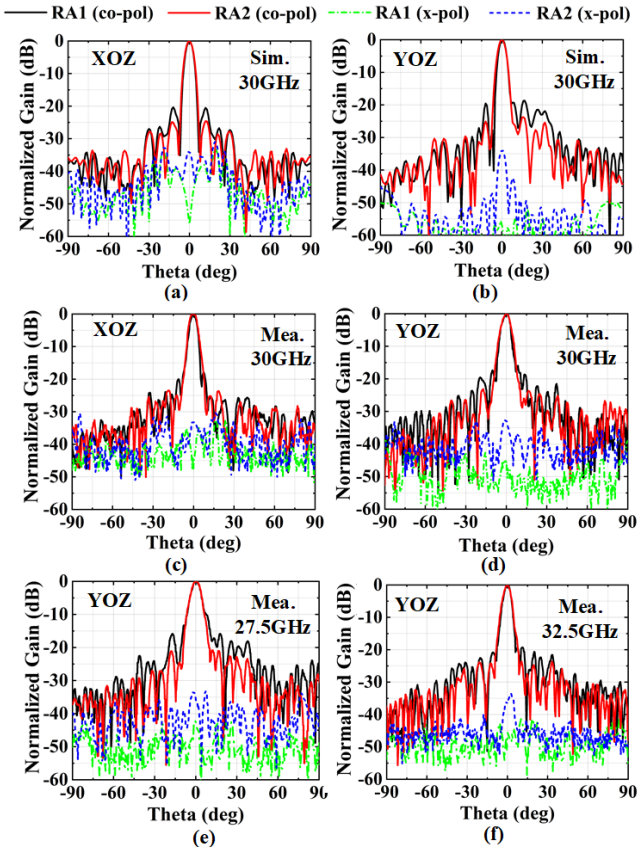

FIGURE 10. Simulated radiation patterns at 30 GHz for MFM RA antennas with phase control only (RA1) and both amplitude and phase control (RA2) in (a) XOZ plane and (b) YOZ plane. Measured radiation patterns for RA1 and RA2 (c) at 30 GHz in XOZ plane, (d) at 30 GHz in YOZ plane, (e) at 27.5 GHz in YOZ plane, (f) at 32.5 GHz in YOZ plane.

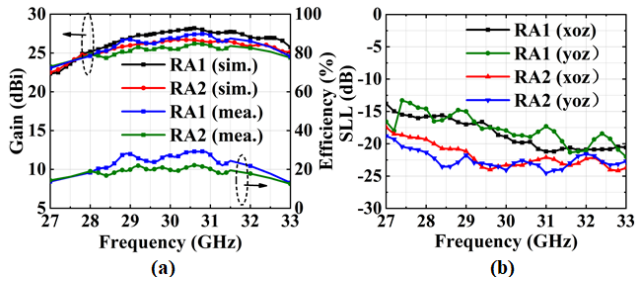

FIGURE 11. (a) Simulated and measured gains and aperture efficiencies for the two MFM RA antennas. (b) Measured SLLs of the two RA antennas with or without the amplitude control in XOZ plane and YOZ plane.

In the XOZ and YOZ planes, the simulated and measured SLLs for TA2 are -29.2 dB/-28.7 dB and -29.2 dB/-27.8 dB, respectively. In contrast, the corresponding SLLs for TA1 are comparatively higher at -23.2 dB/-22.2 dB and -22.6 dB/-22.7 dB, respectively. This indicates a significant reduction in SLLs, approximately 6 dB, with the incorporation of amplitude control. Additionally, the CPLs for both TA antennas are observed to be lower than their respective SLLs, as depicted in Fig. 8. Figs. 8(e) and (f) depict radiation patterns in the YOZ plane at 27.5 GHz and 32.5 GHz, respectively, which are the lower and upper limits of the operation band. It is evident that the SLLs at both 27.5 dB and 32.5 GHz are below -22 dB, demonstrating the wideband low-SLL performance. Fig. 9(a) provides a comprehensive comparison of the simulated and measured gains, as well as the aperture efficiencies for the two TA antennas. Despite a slight reduction, the gains and aperture efficiencies of TA2 remain competitive with those of TA1. Specifically, the peak gains for TA1 are measured at 27.8 dBi (simulated: 28.3 dBi), whereas for TA2, they are recorded at 26.4 dBi (simulated: 26.7 dBi). Correspondingly, the measured aperture efficiencies for TA1 and TA2 are 28.2% and 23.5%, respectively. Fig. 9(b) illustrates the SLLs over frequency for both TA antennas. The measurements reveal a remarkable reduction in SLL over a wide bandwidth, spanning from 26 GHz to 32 GHz, achieved through amplitude control. This reduction, however, comes at the cost of a marginal decrease in gain.

B. Reflectarray Antennas with MFMs

As depicted in Fig. 6(a), RA antenna configuration comprises an x-polarized WR-28 feed horn and a metasurface reflectarray utilizing the reflection mode of the MFM, as detailed in Section II-A. To mitigate feed blockage, an offset feed is adopted and positioned in the YOZ plane with an offset angle of 20º. The designed beam direction is set at 0º along the z-axis. The primary objective of amplitude control is to achieve SLLs less than -25 dB. The metasurface reflectarray consists of 30 × 30 elements, measuring 120 mm × 120 mm × 1 mm (equivalent to 12λ × 12λ × 0.1λ at 30 GHz). The F/D value is maintained at 0.83. Two distinct RA antennas are designed for comparison: one with phase control only (RA1) and another incorporating both amplitude and phase control (RA2). In RA1, the rotation angles of all DSRs on the metasurface are set to 0° or 90°. The required compensation phase distribution on the metasurface is computed using (4), and the discretized version is visualized in Fig. 6(b). Conversely, RA2 integrates amplitude control using the strategy outlined in Section III-B to attain an SLL less than -25 dB. The calculated amplitude distribution for RA2 is presented in Fig. 6(c). Subsequently, comprehensive simulations, fabrications, and measurements are conducted for both RA antennas separately.

Fig. 10 illustrates the simulated and measured radiation patterns for the two RA antennas at 30 GHz. In the XOZ plane and YOZ plane, the measured SLLs for RA2 are observed to be -23.1 dB and -23.8 dB, respectively, whereas for RA1, the corresponding SLLs are higher at -18.9 dB and -17 dB, respectively. This signifies a notable reduction of over 4 dB in SLL achieved through amplitude control. Figs. 10(e) and (f) show radiation patterns in the YOZ plane at 27.5 GHz and 32.5 GHz, respectively. It is observed that the SLLs at 27.5 GHz slightly deteriorate while those at 32.5 GHz are still close to -20 dB.

In Fig. 11(a), a comprehensive comparison of the simulated and measured gains, as well as the aperture efficiencies for the two RA antennas, is presented. The measured peak gains for

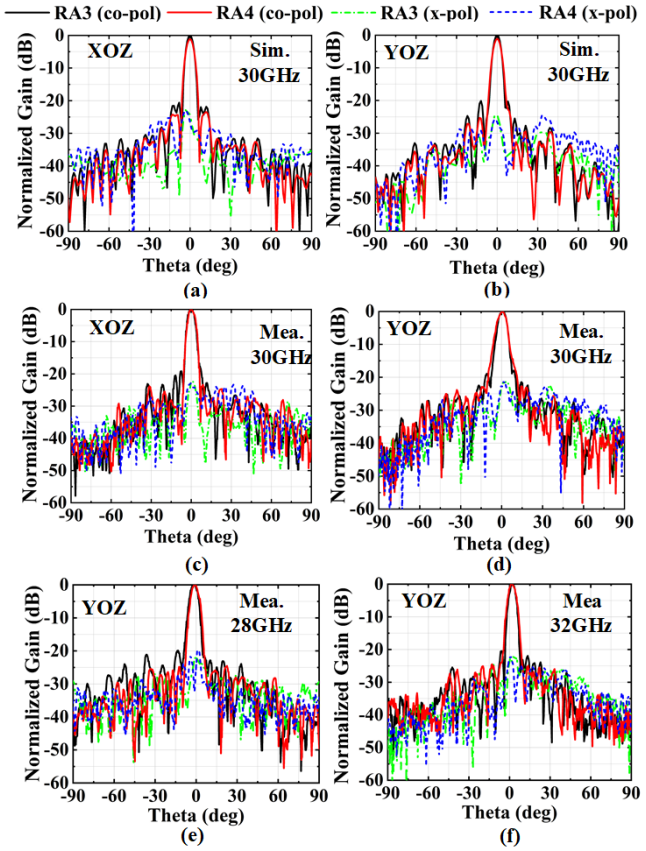

FIGURE 12. Simulated radiation patterns at 30 GHz for the FRM RA antennas with phase control only (RA3) and both amplitude and phase control (RA4) in (a) XOZ plane and (b) YOZ plane. Measured radiation patterns for RA3 and RA4 (c) at 30 GHz in XOZ plane, (d) at 30 GHz in YOZ plane, (e) at 28 GHz in YOZ plane, (f) at 32 GHz in YOZ plane.

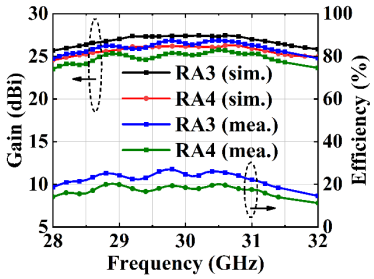

FIGURE 13. Simulated and measured gains and aperture efficiencies for the two FRM RA antennas.

RA1 and RA2 are determined to be 27.5 dBi and 26.2 dBi, respectively, with corresponding aperture efficiencies of 29.2% and 22.1%, respectively. The 3-dB gain bandwidth for the RA2 antenna extends from 28.7 to 33 GHz, representing a 14.4% bandwidth. While the amplitude control results in a reduction of SLL by over 3 dB, there is a slight decrease in gain.

C. Reflectarray Antennas with FRMs

For comparative analysis, RA antennas based on full reflection metasurfaces (FRMs), as detailed in Section II-B, are developed using the same methods and strategies outlined in Section IV-B. Phase control only is implemented in RA3, where all SSRs have a fixed rotation angle of ±45°. In contrast, RA4 incorporates both amplitude and phase control, allowing for variable rotation angles of SSRs to enable control over co-polarization amplitude and achieve an SLL < -25 dB.

Fig. 12 illustrates the simulated and measured radiation patterns for the two FRM RA antennas at 30 GHz. The measured SLLs in the XOZ and YOZ planes for RA4 are -22.7 dB and -23.8 dB, respectively. Conversely, for RA3, the corresponding SLLs are -18 dB and -19.2 dB, respectively. The introduction of amplitude control results in a reduction of approximately 3 dB in SLLs. Figs. 12(e) and (f) display radiation patterns in the YOZ plane at 27 GHz and 32 GHz, respectively. The SLLs at both 27.5 GHz and 32.5 GHz maintain the similar level to those at 30 GHz.

In Fig. 13, a detailed comparison of the simulated and measured gains, along with the aperture efficiencies for RA3 and RA4, is presented. The measured peak gains for RA3 and RA4 are determined to be 26.9 dBi and 25.6 dBi, respectively. The measured aperture efficiencies for RA3 and RA4 are 25.9% and 20.1%, respectively.

TABLE 1. Measured results of the proposed array antennas

@ 30GHz		Gain (dBi)	SLL (dB)	CPL (dB) [a]	AE (%) [b]
TA	TA1	27.3	-22.2	-26.5	29.7
	TA2	25.8	-27.8	-25.1	21.0
MFM RA	RA1	27	-17	-35.2	27.7
	RA2	25.4	-23.1	-30.4	19.2
FRM RA	RA3	25.9	-18	-22.1	21.5
	RA4	24.6	-22.7	-21.2	15.9

[a]CPL denotes the cross-polarization level. [b]AE corresponds to the peak aperture efficiency.

D. Discussion

All simulated and measured results for MFM TA, MFM RA, and FRM RA antennas exhibit commendable agreement, albeit slight discrepancies attributable to measurement noise, fabrication accuracy, and assembly errors. These results robustly affirm the effectiveness of the high-gain, low-SLL design strategy for TA and RA antennas and underscore the superior performance of multifunctional metasurfaces. The multifunctional metasurfaces exhibit advanced features such as wideband coverage, high efficiency, and independent control of amplitude and phase in both reflection and transmission modes.

The summarized measured results in Table 1 validate that, while amplitude control effectively reduces SLLs across all three antenna cases, there is a trade-off with slight reductions in gain. Notably, MFM RA antennas exhibit significantly lower cross-polarization levels compared to FRM RA antennas. This disparity arises from the inherent generation of low-level cross-polarization waves by the grating on the MFM surface. In contrast, the CPLs of FRM antennas are contingent on the cross-polarization conversion efficiency of the FRM, resulting in higher CPLs.

TABLE 2. Comparison between this work and the references

Ref.	Aperture Size (λ^3)	Freq. (GHz)	F/D	Gain (dBi)	SLL (dB)	CPL (dB) [a]	AE [b]	3-dB Gain Bandwidth [c]	3-dB SLL reduction Bandwidth [d]	Type	Method
[24]	9.7×9.7×1.25	28	0.5	23.4	-23.4	≈ -20	18.6%	10.9%	10.9%	CP TA [e]	Phase and amplitude
[29]	4.3×4.3×0.1	10	0.64	17.6	-22.6	-12.3	25%	24% (1-dB)	23% (2-dB)	LP RA	Phase and amplitude
[30]	7×7×0.07	14	0.53	21.8	≈-23.5	≈ -13	26%	8.7% (1-dB)	8.5%	CP RA	Phase and amplitude
[32]	14×14×0.007	10	-	25.5	-19.8	-28.6	15%	15% (1-dB)	-	LP TA	Phase
				25.0	-18.4	-19.5	14%	14% (1-dB)	-	LP RA	
[33]	5.5×5.5×0.15	10	0.27	21.4	≈-18	≈-35	36.3%	-	-	LP TA	Phase
				20	≈-15	≈-25	37.4%	-	-	LP RA	
This work	12×12×0.1	30	0.83	26.4	-27.8	-25.1	23.5%	20%	20.7%	LP TA	phase and amplitude
				26.2	-23.1	-30.4	22.1%	14.4%	18.5%	LP RA	

[a]CPL denotes the cross-polarization level. [b]AE corresponds to the peak aperture efficiency. [c]3-dB Gain Bandwidth describes the frequency range over which the antenna's gain decreases by no more than 3 dB from its peak gain. [d]3-dB SLL reduction Bandwidth refers to the frequency range over which SLLs are effectively reduced by more than 3 dB after applying amplitude control. [e]LP and CP Refer to the linearly-polarized and circularly polarized, respectively.

The configuration of our MFMs inherently yields low CPLs. With an MFM, redundant power resulting from amplitude control passes through the metasurface and scatters in the space opposite the reflection plane. In FRM RA antennas, however, redundant power is converted into cross-polarization waves in the reflection space, leading to increased CPLs. As indicated in Table 1, the peak CPL with MFM RA is lower than the corresponding SLL, whereas that of FRM RA is higher than the SLL.

For the TA antenna, though the CPL is slightly greater than the SLL, it remains acceptable and can be further reduced by optimizing the slots of the metasurface gratings.

Table 2 provides a comprehensive performance comparison between the low- SLL TA and MFM RA antennas presented in this study and previously reported low-SLL TA or RA antennas from existing literature. An innovative circularly polarized TA design introduced in [24] aims to mitigate SLL by incorporating a stacked structure consisting of a phase-adjustable metasurface and an amplitude-adjustable metasurface. However, this stacked approach increases the profile of the TA. In contrast, our proposed TA and RA antennas leverage a metasurface with simultaneous amplitude and phase modulations, presenting a more streamlined solution. In measurement, the proposed TA and RA antennas exhibit the lowest SLL and a broad SLL reduction bandwidth compared to other designs reported in [24], [29]-[30] at the center frequency.

Moreover, in [29]-[30], the method of amplitude control involves converting abundant power into cross-polarization, resulting in an exceptionally high cross-polarization level. In contrast, our proposed RA employs a distinct approach where the metasurface modulates the reflected amplitude and transmits redundant power into the space opposite the working space. Consequently, the RA in this study achieves the lowest CPL when suppressing SLL, distinguishing it from other designs. This comparative analysis substantiates the excellent performance of the proposed array antennas. Finally, the amplitude and phase of the MFM can be controlled across a wide bandwidth, displaying a linearly varied phase and nearly unchanged amplitude. As evident in Table II, the high-gain and low-SLL performance can be consistently achieved within a broad frequency range. Consequently, the MFM introduced in this study emerges as a compelling candidate for high-gain, low-SLL antenna designs.

V. CONCLUSION

The successful application of a metasurface, enabling independent amplitude and phase control in both reflection and transmission modes, has paved the way for the design of wideband, high-gain, low-SLL, and low-CPL reflectarray and transmitarray antennas. The proposed metasurface effectively tailors the amplitude of incident fields, strategically placing redundant fields opposite the working space. This design choice yields exceptional performance characterized by low SLL and CPL within the working space for the RA/TA antennas. The validity of these claims is substantiated through comprehensive simulations and experimental validations. Our innovative work represents a significant stride in crafting high-performance multifunctional antenna systems tailored for contemporary and future wireless communication networks.

ACKNOWLEDGMENT

This work was supported by National Natural Science Foundation of China (NSFC) (under grants #62071187, 62071125, 62301162), Natural Science Foundation of Fujian Province, China (under grant #2023J01058), and the Industry-Education Cooperation Project in Fujian Province, China (under grant #2022H6018), Fujian Province Major Special

Topic Project (under grant #2022HZ026007). (Corresponding authors: Yuehe Ge)

REFERENCES

[1] W. Kummer, A. Villeneuve, T. Fong, and F. Terrio, "Ultra-low sidelobes from time-modulated arrays," *IEEE Trans. Antennas Propag.*, vol. 11, no. 6, pp. 633-639, Nov. 1963.

[2] D. M. Pozar, and B. Kaufman, "Design considerations for low sidelobe microstrip arrays," *IEEE Trans. Antennas Propag.*, vol. 38, no. 8, pp. 1176-1185, Aug. 1990.

[3] C. Granet, T. S. Bird, and G. L. James, "Compact multimode horn with low sidelobes for global Earth coverage," *IEEE Trans. Antennas Propag.*, vol. 48, no. 7, pp. 1125-1133, July 2000.

[4] X. Chen, and Y. Ge, "Enhancing the radiation performance of a pyramidal horn antenna by loading a subwavelength metasurface," *IEEE Access*, vol. 5, pp. 20164-20170, Oct. 2017.

[5] Y. Liu, H. Yang, Z. Jin, F. Zhao, and J. Zhu, "Compact Rotman lens-fed slot array antenna with low sidelobes," *IET Microw. Antennas Propag.*, vol. 12, no. 5, pp. 656-661, Apr. 2018.

[6] J. Xu, W. Hong, P. Chen, and K. Wu, "Design and implementation of low sidelobe substrate integrated waveguide longitudinal slot array antennas," *IET Microw. Antennas Propag.*, vol. 3, no. 5, pp. 790-797, Aug. 2009.

[7] P. Kumar, A. Kedar and A. K. Singh, "Design and development of low-cost low sidelobe level slotted waveguide antenna array in X-band," *IEEE Trans. Antennas Propag.*, vol. 63, no. 11, pp. 4723-4731, Nov. 2015.

[8] H. Chu, P. Li, and Y. Guo, "A beam-shaping feeding network in series configuration for antenna array with cosecant-square pattern and low sidelobes," *IEEE Antenna Wirel. Propag. Lett.*, vol. 18, no. 4, pp. 742-746, Apr. 2019.

[9] F. Kuo, and R. Hwang, "High-isolation X-Band marine radar antenna design," *IEEE Trans. Antenna Propag.*, vol. 62, no. 5, pp. 2331-2337, May 2014.

[10] H. Mardani, J. Nourinia, C. Ghobadi, M. Majidzadeh, and B. Mohammadi, "A compact low-side lobes three-layer array antenna for X-band applications," *AEU-Int. J. Electron. Commun.*, vol. 99, pp. 1-7, 2019.

[11] N. Yu, P. Genevet, M. A. Kats, F. Aieta, J. P. Tetienne, F. Capasso, and Z. Gaburro, "Light propagation with phase discontinuities: generalized laws of reflection and refraction," *Science*, vol. 334, no. 6054, pp. 333-337, Oct. 2011.

[12] P. F. McManamon, P. J. Bos, M. J. Escuti, J. Heikenfeld, S. Serati, H. Xie, and E. A. Watson, "A review of phased array steering for narrow-band electrooptical systems," *Proceedings of the IEEE*, vol. 97, no. 6, pp. 1078-1096, Jun. 2009.

[13] J. Huang, and J.A. Encinar, *Reflectarray antennas*. Hoboken, NJ, USA: Wiley-IEEE Press, 2008.

[14] S. V. Hum and J. Perruisseau-Carrier, "Reconfigurable reflectarrays and array lenses for dynamic antenna beam control: A Review," *IEEE Trans. Antennas Propag.*, vol. 62, no. 1, pp. 183-198, Jan. 2014.

[15] X. Gao, X. Han, W. Cao, H. Li, H. Ma, and T. J. Cui, "Ultrawideband and high-efficiency linear polarization converter based on double V-shaped metasurface," *IEEE Trans. Antenna Propag.,* vol. 63, no. 8, pp. 3522-3530, Aug. 2015.

[16] Y. Chen, Y. Ge, and T. S. Bird, "An offset reflectarray antenna for multipolarization applications," *IEEE Antenna Wirel. Propag. Lett.*, vol. 15, pp. 1-1, 2016.

[17] J. R. Reis, M. Vala, and R. F. S. Caldeirinha, "Review paper on transmitarray antennas," *IEEE Access,* vol. 7, pp. 94171-94188, 2019

[18] H. Li, G. Wang, H. Xu, T. Cai, and J. Liang, "X-Band phase-gradient metasurface for high-gain lens antenna application," *IEEE Trans. Antenna Propag.,* vol. 63, no. 11, pp. 5144-5149, Nov. 2015.

[19] Y. Ge, C. Lin, and Y. Liu, "Broadband folded transmitarray antenna based on an ultrathin transmission polarizer," *IEEE Trans. Antenna Propag.*, vol. 66, no. 11, pp. 5974-5981, Nov. 2018.

[20] M. Feng, Y. Li, J. Wang, Q. Zheng, S. Sui, C. Wang, H. Chen, H. Ma, S. Qu, and J. Zhang, "Ultra-wideband and high-efficiency transparent coding metasurface," *Appl. Phys. A-Mat. Sci. Process.,* vol. 124, no. 9, Sep. 2018.

[21] E. Erfani, M. Niroo-Jazi and S. Tatu, "A high-gain broadband gradient refractive index metasurface lens antenna," *IEEE Trans. Antenna Propag.*, vol. 64, no. 5, pp. 1968-1973, May 2016.

[22] C. Song, L. Pan, Y. Jiao, and J. Jia. "A high-performance transmitarray antenna with thin metasurface for 5G communication based on PSO (particle swarm optimization)," *Sensors*, vol.20, no.16, pp. 4598-4605, Aug. 2020.

[23] Q. Zheng, Y. Li, Y. Han, Y. Jing, M. Feng1, Y. Pang, J. Wang, H. Ma, S. Qu, and J. Zhang, "Ultra-wideband side-lobe level suppression using amplitude-adjustable metasurfaces," *J. Phys. D-Appl. Phys.*, vol. 52, no. 6, pp. 065102, Feb. 2019.

[24] Q. Lou and Z. Chen, "Sidelobe suppression of metalens antenna by amplitude and phase controllable metasurfaces," *IEEE Trans. Antennas Propag.*, vol. 69, no. 10, pp. 6977-6981, Oct. 2021.

[25] M. Kim, A. M. H. Wong, and G. V. Eleftheriades, "Optical Huygens' metasurfaces with independent control of the magnitude and phase of the local reflection coefficients," *Phys. Rev. X,* vol. 4, no. 4, pp. 041042, Dec. 2014.

[26] S. Jia, X. Wan, P. Su, Y. Zhao, and T. J. Cui, "Broadband metasurface for independent control of reflected amplitude and phase," *AIP Adv.*, vol. 6, no. 4, pp. 045024, Apr. 2016.

[27] L. Liu, X. Zhang, M. Kenney, X. Su, N. Xu, C. Ouyang, Y. Shi, J. Han, W. Zhang, S. Zhang, "Broadband metasurfaces with simultaneous control of phase and amplitude," *Adv. Mat.,* vol. 26, no. 29, pp. 5031-5036, Aug. 2014.

[28] H. Li, G. Wang, T. Cai, H. Hou, and W. Guo, "Wideband transparent beam-forming metadevice with amplitude- and phase-controlled metasurface," *Phys. Rev. Appl.*, vol. 11, no. 1, pp. 014043, Jan. 2019.

[29] H. Li, G. Wang, T. Cai, J. Liang, and X. Gao, "Phase- and amplitude-control metasurfaces for antenna main-lobe and sidelobe manipulations," *IEEE Trans. Antenna Propag.*, vol. 66, no. 10, pp. 5121-5129, Oct. 2018.

[30] W. Guo, G. Wang, X. Luo, K. Chen, H. Li, and Y. Feng, "Dual-phase hybrid metasurface for independent amplitude and phase control of circularly polarized wave," *IEEE Trans. Antenna Propag.*, vol. 68, no. 11, pp. 7705-7710, Nov. 2020.

[31] H. Xu, S. Tang, G. Wang, T. Cai, W. Huang, Q. He, S. Sun, and L. Zhou, "Multifunctional microstrip array combining a linear polarizer and focusing metasurface," *IEEE Trans. Antenna Propag.*, vol. 64, no. 8, pp. 3676-3682, Aug. 2016.

[32] F. Yang, R. Deng, S. Xu, and M. Li, "Design and experiment of a near-zero-thickness high-gain transmit-reflect-array antenna using anisotropic metasurface," *IEEE Trans. Antenna Propag.*, vol. 66, no. 6, pp. 2853-2861, Jun. 2018.

[33] T. Cai, G. Wang, X. Fu, J. Liang, and Y. Zhuang, "High-efficiency metasurface with polarization-dependent transmission and reflection properties for both reflectarray and transmitarray," *IEEE Trans. Antenna Propag.*, vol. 66, no. 6, pp. 3219-3224, Jun. 2018.

[34] Y. Wang, Y. Ge, Z. Chen, X. Liu, J. Pu, K. Liu, H. Chen, and Y. Hao, "Broadband high-efficiency ultrathin metasurfaces with simultaneous independent control of transmission and reflection amplitudes and phases," *IEEE Trans. Microw. Theory. and Tech.*, vol. 70, no. 1, pp. 254-263, Jan. 2022.

[35] Y. Wang, Y. Ge and Z. D. Chen, "A Broadband High-efficiency Multifunctional Ultrathin Metasurfaces," in *Proc. Photon. Electromagn. Res. Symp. (PIERS)*, Hangzhou, China, 2022, pp. 954-960.

[36] Robert Mailloux, *Phased Array Antenna Handbook*, 2nd ed. Norwood, MA: Artech House, 2005.